Chemical Science

ROYAL SOCIETY OF CHEMISTRY

EDGE ARTICLE

View Article Online
View Journal | View Issue

Cite this: *Chem. Sci.*, 2025, **16**, 1265

All publication charges for this article have been paid for by the Royal Society of Chemistry

Received 26th October 2024
Accepted 4th December 2024

DOI: 10.1039/d4sc07257j

rsc.li/chemical-science

Electronic regulation of single-atomic Ti sites on metal hydroxide for boosting photocatalytic CO_2 reduction†

Ning-Yu Huang,‡[a] Bai Li,‡[c] Duojie Wu,[d] Di Chen,[a] Yu-Tao Zheng,[a] Bing Shao,[a] Wenjuan Wang,[a] Meng Gu,[d] Lei Li *[c] and Qiang Xu *[ab]

Photocatalytic CO_2 reduction is considered a sustainable method to address energy and environmental issues by converting CO_2 into fuels and chemicals, yet the performance is still unsatisfactory. Single atom catalysts hold promising potential in photocatalysis, but the selection of metal species is still limited, especially in early transition metals. Herein, inspired by the structure of anatase TiO_2, single Ti sites were successfully incorporated into a metal hydroxide support for the first time *via* cationic defects, significantly enhancing the photocatalytic performance by more than 30 times (from 0.26 to 8.09 mmol g^{-1} h^{-1}). Based on the theoretical calculation and *in situ* characterization, the enhancement of photocatalytic performance can be attributed to the regulation of the electronic structure by the introduction of atomically dispersed Ti sites, leading to stronger binding with intermediates and enhanced charge transfer.

Introduction

The overuse of non-renewable fossil fuels has caused excessive atmospheric CO_2 emission, which has become one of the urgent topics globally.[1–6] Photocatalytic CO_2 reduction, utilizing sustainable solar energy to convert CO_2 into fuels and chemicals (*e.g.*, carbon monoxide, formic acid, and methane), is considered a promising method to address the energy crisis and environmental issues.[7–16] Because of the inertness of CO_2 molecules and insufficient utilization of active sites in photocatalysts, the current performances for photocatalytic CO_2 reduction are far from satisfactory towards practical applications.[17–20] Therefore, developing novel catalysts with efficient active sites is of great significance but challenging as well. Single-atom catalysts (SACs), uniformly dispersing metal atoms on appropriate substrates, have shown high catalytic efficiency and product selectivity towards CO_2 reduction because of their open active sites and unique electronic properties.[21–29] Among reported literature, late transition metals (*e.g.*, Cu, Co, Pt, Ir, and Pd) have been well-studied as active metal sites for various catalytic applications.[30–33] However, very few early transition metals (groups 3–7) have been considered for the construction of SACs, which normally possess variable oxidation states, strong metal-carrier interaction and electron transfer efficiency.[34] Developing SACs with early transition metal species can open up new opportunities for the exploration of efficient photocatalysts in CO_2 reduction.

Because of its abundance, non-toxicity and unique redox ability, titanium (Ti) has been widely applied as a component of many classical photocatalysts (*e.g.*, TiO_2, $SrTiO_3$, *etc.*) for decades.[35–37] Among them, anatase and rutile, as two different phases of TiO_2, have different coordination configurations and electronic structures, leading to distinct catalytic properties. Compared to rutile TiO_2, the more distorted TiO_6 octahedron and different structural rearrangements in anatase TiO_2 can offer a larger band gap and stronger redox driving force, as well as higher surface area, more active sites (such as oxygen vacancies) and more efficient charge separation, thus exhibiting better photocatalytic activity.[38] Therefore, transplanting the isolated TiO_6 octahedron of anatase TiO_2 in suitable supports to construct SACs can trigger the modification of electronic structures and enhance the performance in various solar driven applications.[39] For example, Shi and coworkers anchored Ti single atoms on reduced graphene oxide for tuning the electronic properties and minimizing the charge resistance,

[a]*Shenzhen Key Laboratory of Micro/Nano-Porous Functional Materials (SKLPM), SUSTech-Kyoto University Advanced Energy Materials Joint Innovation Laboratory (SKAEM-JIL), Department of Chemistry, Department of Materials Science and Engineering, Southern University of Science and Technology, Shenzhen 518055, China. E-mail: xuq@sustech.edu.cn*

[b]*Institute for Integrated Cell-Material Sciences (WPI-iCeMS), Kyoto University, Yoshida, Sakyo-ku, Kyoto 606-8501, Japan. E-mail: xu.qiang@icems.kyoto-u.ac.jp*

[c]*Shenzhen Key Laboratory of Micro/Nano-Porous Functional Materials (SKLPM), Department of Materials Science and Engineering, Southern University of Science and Technology, Shenzhen 518055, China. E-mail: lil33@sustech.edu.cn*

[d]*Department of Materials Science and Engineering, Guangdong Provincial Key Laboratory of Energy Materials for Electric Power, Southern University of Science and Technology, Shenzhen 518055, China*

† Electronic supplementary information (ESI) available: Experimental methods and characterization data. See DOI: https://doi.org/10.1039/d4sc07257j

‡ N.-Y. Huang and B. Li contributed equally to this work.

resulting in high-performance perovskite solar cells and encouraging further exploration of Ti-based SACs.[40]

Although Ti-based semiconductors have been widely studied in the field of photocatalysis, there is only one example of Ti SACs for photocatalytic CO_2 reduction, in which the single Ti site is coordinated by N atoms of graphitic carbon nitride (g-C_3N_4).[41] Herein, taking advantage of unique electronic properties, we incorporate single-atomic Ti sites into defective nickel hydroxide substrates to afford an earth-abundant SAC, significantly promoting the performance of photocatalytic CO_2 reduction to CO (Fig. 1a). Nickel hydroxide ($Ni(OH)_2$), as a typical transition metal hydroxide, exhibits a two-dimensional structure and the distorted NiO_6 octahedron coordination mode similar to anatase TiO_2, making it suitable for the construction of Ti SACs.[42–44] By creating cationic defects, Ti atoms tend to coordinate with dangling O atoms to fill the vacancies and the single metal sites can be atomically dispersed into $Ni(OH)_2$ with a high loading amount, which is a feasible method for preparing SACs.

Results and discussion

According to the previous literature, the metal ions of metal hydroxides can be dissolved out by coordinating with appropriate ligands or solvents, inducing cationic vacancies in the pristine materials.[45] Therefore, treated in a mixed solution of *N*,*N*-dimethylformamide (DMF)/ethanol/H_2O, defective $Ni(OH)_2$ (d-$Ni(OH)_2$) was synthesized from $Ni(OH)_2$ nanosheets *via* a simple solvothermal method, showing lower peak intensity of PXRD patterns compared to pristine $Ni(OH)_2$ without additional compounds (Fig. 1b and S1†). As shown in the scanning electron microscopy (SEM) and transmission electron microscopy (TEM) images (Fig. S2 and S3†), d-$Ni(OH)_2$ exhibited sheet-like morphology like $Ni(OH)_2$ with cavities of 1–2 nm, indicating the creation of defects after solvothermal treatment. Moreover, the dissolved Ni^{2+} ions in mother liquor were determined by inductively coupled plasma mass spectrometry (ICP-MS, Table S1†), in which *ca.* 0.18% of Ni ions in pristine $Ni(OH)_2$ was dissolved. Based on the X-ray photoelectron spectroscopy (XPS), the peaks in the Ni 2p spectrum (Fig. S4†) of d-$Ni(OH)_2$ shifted to higher binding energy compared to pristine $Ni(OH)_2$, consistent with the result from Ni K-edge X-ray absorption near-edge structure (XANES) spectra (Fig. S5a†), which can be assigned to the increased valence state of Ni caused by the existence of cationic defects. More importantly, the Fourier transform extended X-ray absorption fine structure (FT-EXAFS) spectra showed longer Ni–Ni bond length for d-$Ni(OH)_2$ compared to pristine $Ni(OH)_2$ (Fig. S5b†), which was attributed to the local extension of the neighboring Ni sites due to the existence of Ni^{2+}-based cationic defects. Furthermore, zeta potential measurements revealed that compared to positively charged $Ni(OH)_2$, d-$Ni(OH)_2$ got negatively charged after solvothermal treatment (Fig. S6†), further suggesting the successful construction of defective $Ni(OH)_2$ as a substrate for anchoring Ti sites.

With the help of the strong interaction between Ti ions and dangling oxo species, the $Ti_1/Ni(OH)_2$ SACs were prepared *via* a simple impregnation strategy by stirring in the solution of organic Ti salt. The PXRD pattern of $Ti_1/Ni(OH)_2$ showed enhanced intensity compared to d-$Ni(OH)_2$ without additional peaks of TiO_2 or other Ti-related materials (Fig. 1b). Raman spectra indicated the successful anchoring of Ti sites, showing obvious peaks at 556 and 664 cm^{-1} in $Ti_1/Ni(OH)_2$ corresponding to the Ti–O bonds (Fig. S7†). The loading content of Ti in $Ti_1/Ni(OH)_2$ was determined to be *ca.* 2.06 wt% by using ICP-MS (Table S1†), which is relatively high among the reported

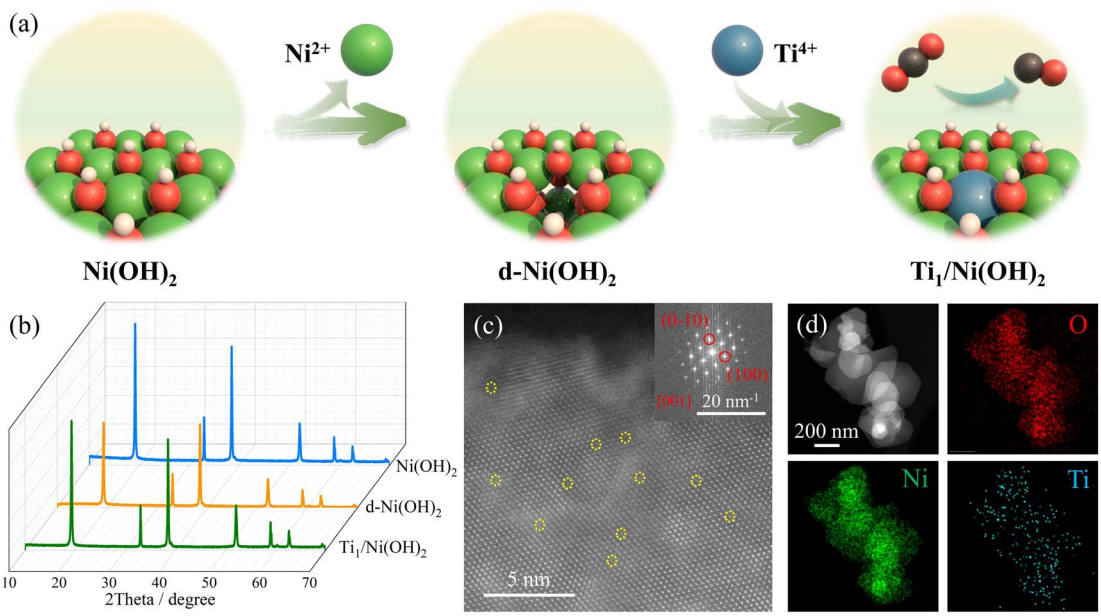

Fig. 1 (a) Schematic illustration of the incorporation of single Ti sites on $Ni(OH)_2$. (b) PXRD patterns of $Ni(OH)_2$, d-$Ni(OH)_2$ and $Ti_1/Ni(OH)_2$. (c) Atomic resolution HAADF-STEM image of $Ti_1/Ni(OH)_2$. The dark spots representing Ti atomic sites were highlighted. The inset shows an FFT pattern corresponding to $Ni(OH)_2$. (d) HAADF-STEM image of $Ti_1/Ni(OH)_2$ and the corresponding elemental mapping images of O, Ni and Ti.

SACs. After introducing higher-valent Ti ions, the Ni 2p XPS spectrum of $Ti_1/Ni(OH)_2$ shifted to higher binding energy compared to that of d-$Ni(OH)_2$ (Fig. S4†), which can be attributed to the effect of electron delocalization, leading to a higher valence state and binding energy for Ni ions. The O 1s XPS spectra showed an observable shift toward higher binding energy for d-$Ni(OH)_2$ (531.1 eV) and even further for $Ti_1/Ni(OH)_2$ (531.5 eV), which can be ascribed to a synergy effect of oxygen vacancies and Ti sites. Moreover, according to the electron paramagnetic resonance (EPR) spectra (Fig. S8†), although a small amount of oxygen vacancies appeared (peak at $g = 2.00$) during the construction of cationic defects in d-$Ni(OH)_2$, the oxygen vacancies were mostly filled in $Ti_1/Ni(OH)_2$ accompanied by the introduction of Ti species (peak at $g = 1.98$).[46,47] As shown in the SEM images (Fig. S2†), the sheet-like morphology of $Ni(OH)_2$ remained unchanged after modification and no other Ti particles were formed, further suggesting the atomic dispersion of Ti species. The uniform distribution of Ti atoms was confirmed by the energy-dispersive X-ray spectroscopy (EDS) analysis and elemental mapping (Fig. 1d and S9†), showing a Ti loading amount of 1.66 wt%, which is consistent with the ICP-MS result. Because of the lower atomic number of Ti, the darker spots in the aberration-corrected high-angle annular dark-field scanning transmission electron microscopy (AC-HAADF-STEM) image (yellow circles in Fig. 1c) could be attributed to the Ti single atoms. More importantly, the brightness intensity profiles along different lines all showed single spots with lower intensity corresponding to Ti atomic sites (Fig. S10†), further confirming the presence of Ti single atoms in $Ni(OH)_2$. To better illustrate the single-atomic nature, other group 4 metals (Zr and Hf) were also employed to construct SACs on $Ni(OH)_2$, namely $Zr_1/Ni(OH)_2$ and $Hf_1/Ni(OH)_2$. The uniform dispersion of metal sites was confirmed by PXRD patterns and EDX mapping (Fig. S11–S13†). As shown in the HAADF-STEM images (Fig. S12 and S13†), observable bright spots corresponding to the single-atomic sites in $Zr_1/Ni(OH)_2$ and $Hf_1/Ni(OH)_2$ further demonstrated the general synthesis of early transition metal SACs.

To further investigate the local coordination environment of the Ti atom, XPS and X-ray absorption spectroscopy (XAS) were conducted. According to the Ti 2p XPS spectra of $Ti_1/Ni(OH)_2$ (Fig. 2a), the characteristic peaks at a binding energy of 458.5 and 464.4 eV were assigned to Ti $2p_{3/2}$ and Ti $2p_{1/2}$, respectively, indicating an approximate +4 valence state of Ti ions in $Ti_1/Ni(OH)_2$, which is further determined to be +3.5 by the linear fitting results based on the corresponding XANES spectra (Fig. 2b and S14†). More importantly, $Ti_1/Ni(OH)_2$ displayed distinct peaks in the pre-edge region of the Ti XANES spectrum compared to anatase TiO_2 (the inset of Fig. 2b), indicating the absence of anatase TiO_2 in this material. Furthermore, the FT-EXAFS spectra of $Ti_1/Ni(OH)_2$ exhibited the main peak located at *ca.* 1.56 Å (Fig. 2c), which can be attributed to the Ti–O scattering path similar to that of TiO_2. In the meantime, the signal of Ti–Ti at *ca.* 2.52 Å was significantly lower compared to that of both TiO_2 and Ti foil, further demonstrating the high dispersion of Ti sites. Based on the EXAFS fitting analysis for $Ti_1/Ni(OH)_2$ (Fig. 2d and Table S2†), the coordination number of Ti atoms in $Ti_1/Ni(OH)_2$ was determined to be 5.7, suggesting that the Ti atom is octahedrally coordinated in place of the Ni atom. Compared to those of Ti foil and TiO_2, the wavelet transformation (WT) plot of $Ti_1/Ni(OH)_2$ showed the WT maximum at 1.3 $Å^{-1}$, ascribed to Ti–O bonding, while no intensity maximum was observed for Ti–Ti (Fig. 2e–g). Overall, combined with XAS, HAADF-STEM and a series of characterization methods, it was demonstrated that the monodisperse Ti sites were successfully anchored on the defective $Ni(OH)_2$ substrate created by the solvothermal method.

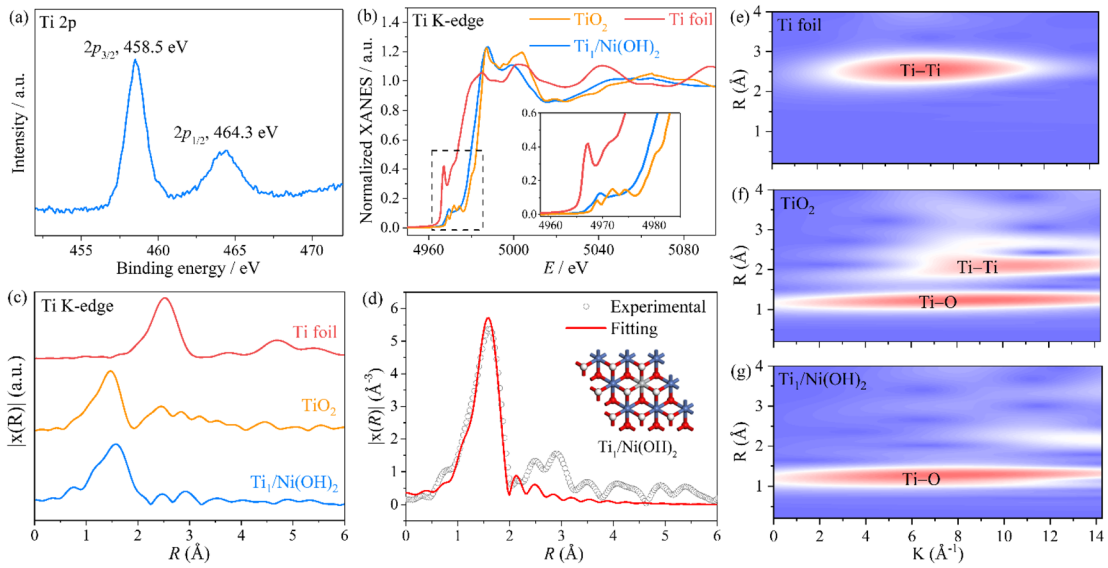

Fig. 2 (a) Ti 2p XPS spectrum of $Ti_1/Ni(OH)_2$. (b) Ti K-edge XANES spectra of $Ti_1/Ni(OH)_2$, TiO_2 and Ti foil. The inset highlights the near-edge absorption energy. (c) Ti K-edge EXAFS spectra of $Ti_1/Ni(OH)_2$, TiO_2 and Ti foil and (d) the corresponding EXAFS fitting curve at *R*-space and the structural model (inset) of $Ti_1/Ni(OH)_2$. (e–g) WT-EXAFS contour plots of Ti foil, TiO_2 and $Ti_1/Ni(OH)_2$, respectively.

To evaluate the critical role of single Ti sites, photocatalytic CO_2 reduction experiments were conducted under LED irradiation ($\lambda > 410$ nm), using 1,3-dimethyl-2-phenyl-2,3-dihydro-1*H*-benzo[*d*]imidazole (BIH) as a sacrificial agent and $[Ru(phen)_3]Cl_2$ (phen = 1,10-phenanthroline) as a photosensitizer. The gaseous and liquid products evolved in the reaction system were detected by gas chromatography (GC) and ^1H nuclear magnetic resonance (^1H NMR), respectively. After light irradiation, CO and H_2 were detected as the main products and no other liquid-phase product was detected in the catalytic system (Fig. S15 and S16†). Prior to the detailed evaluation of photocatalytic performance, the best performance of $Ti_1/Ni(OH)_2$ was optimized by varying its synthetic conditions, including the amount of Ti precursor, synthetic time and temperature of d-$Ni(OH)_2$ (Fig. S17†). During 4 h of light irradiation, the amount of CO and H_2 increased linearly with time by using $Ti_1/Ni(OH)_2$ as a catalyst (Fig. 3a), showing a CO production rate of 8.09 mmol g^{-1} h^{-1} with excellent CO selectivity as high as 96.5%, which is comparable to the reported benchmark performance (Table S3†). In comparison, the CO production rates of $Ni(OH)_2$ and d-$Ni(OH)_2$ were 0.80 and 0.26 mmol g^{-1} h^{-1}, respectively (Fig. 3b). The photocatalytic activity of $Ti_1/Ni(OH)_2$ was more than 30 times higher than that of pristine $Ni(OH)_2$, strongly suggesting that the introduction of single Ti sites played a significant role in promoting the photocatalytic performance. Moreover, $Ti_1/Ni(OH)_2$ greatly outperformed anatase TiO_2 or the physical mixture of $Ni(OH)_2$ and TiO_2 (Fig. S18†), further demonstrating the importance of the synergistic effect in this Ti-metal hydroxide system.

During the cyclic experiments, $Ti_1/Ni(OH)_2$ can maintain 98% of the initial performance after 5 consecutive runs (Fig. 3c), indicating its excellent photocatalytic stability, which was also confirmed by the PXRD patterns, SEM images and ICP-MS measurements of the sample after photocatalysis (Fig. S19 and Table S1†). According to the control experiments, only a negligible product can be observed in the absence of the catalyst, the photosensitizer, the sacrificial agent, CO_2, H_2O and light, indicating the necessity of these conditions for the photocatalytic process (Fig. S20†). To further confirm the carbon source, isotope labeling experiments were conducted by using $^{13}CO_2$ as the feedstock gas. As shown in gas chromatography-mass spectrometry (GC-MS, Fig. 3d), the signal of ^{13}CO (m/z = 29) was clearly observed, demonstrating that CO was generated from the CO_2 feedstock instead of the photosensitizer, the sacrificial agent or the catalyst itself.

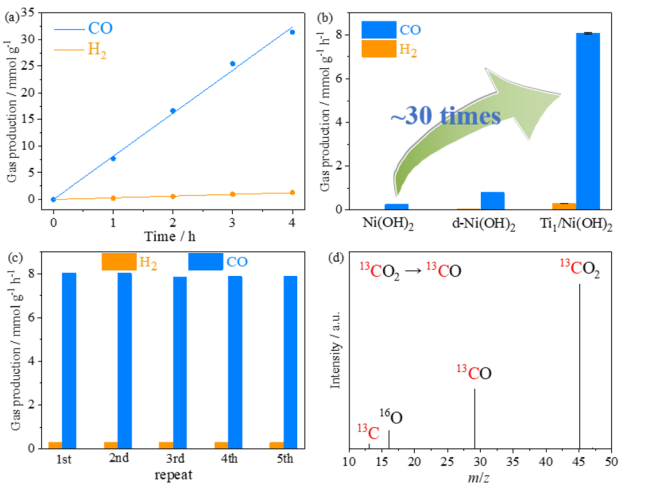

Fig. 3 (a) CO and H_2 production of photocatalytic CO_2 reduction using the catalyst $Ti_1/Ni(OH)_2$. (b) Comparison of the gas production for $Ni(OH)_2$, d-$Ni(OH)_2$ and $Ti_1/Ni(OH)_2$. (c) Recycle experiments of $Ti_1/Ni(OH)_2$. (d) Mass spectra of the gaseous products of photocatalytic CO_2 reduction by using $^{13}CO_2$ as the gas source.

According to the UV-vis spectra (Fig. S21†), after anchoring single Ti sites, $Ti_1/Ni(OH)_2$ exhibited enhanced light absorption in the region of 300–400 nm compared to d-$Ni(OH)_2$ and $Ni(OH)_2$. To better reveal the charge transfer behavior, photoluminescence (PL) spectra and electrochemical impedance spectroscopy (EIS) spectra were measured for $Ti_1/Ni(OH)_2$ and its control samples. Under the excitation at 465 nm, a characteristic emission peak of the excited $Ru(phen)_3Cl_2$ can be observed at *ca.* 570 nm (Fig. S22†), which can be effectively quenched by adding either $Ni(OH)_2$, d-$Ni(OH)_2$ or $Ti_1/Ni(OH)_2$. In particular, the PL intensity with $Ti_1/Ni(OH)_2$ is significantly lower than those with $Ni(OH)_2$ and d-$Ni(OH)_2$, indicating the most efficient charge transfer process for $Ti_1/Ni(OH)_2$. Furthermore, according to the EIS spectra, $Ti_1/Ni(OH)_2$ exhibited the smallest semicircle in the Nyquist plots (Fig. S23†), suggesting the lowest charge transfer resistance and more efficient separation of photogenerated charge carriers, which can well elucidate the best photocatalytic performance for $Ti_1/Ni(OH)_2$.

To gain insight into the enhanced performance of the Ti single atom in the photocatalytic CO_2 reduction, the density functional theory (DFT) method was employed to calculate the free-energy profiles for CO_2 reduction on pristine $Ni(OH)_2$, d-$Ni(OH)_2$ and $Ti_1/Ni(OH)_2$ (Fig. S24†). For both $Ni(OH)_2$ and d-$Ni(OH)_2$, the rate determining steps (RDSs) were the protonation of the CO_2 molecule ($CO_2^* + H^+ + e^- \rightarrow COOH^*$), with free energy changes (DG) of 1.97 eV and 1.85 eV, respectively (Fig. 4a). Anchoring a single Ti site into $Ni(OH)_2$ significantly enhances the adsorption of key intermediates (CO_2^* and $COOH^*$), as indicated by the shorter vertical distance upon adsorption (Fig. S25†). In particular, the strong interaction between CO_2 and $Ti_1/Ni(OH)_2$ leads to a bent adsorption configuration of CO_2 (Fig. S25†), activating C–O bonds and significantly lowering the free energy of corresponding reaction intermediates. Therefore, the RDS for $Ti_1/Ni(OH)_2$ was altered to the dehydration of COOH* ($COOH^* + H^+ + e^- \rightarrow CO^* + H_2O$), of which the ΔG remarkably decreased to 0.56 eV, resulting in increased CO production in photocatalytic CO_2 reduction. To probe the key intermediates and verify the reaction mechanism, *in situ* Fourier transform infrared spectroscopy (FTIR) measurements were conducted using $Ti_1/Ni(OH)_2$ as the photocatalyst (Fig. S26†). Under light irradiation, the peaks at 1542 and 1647 cm^{-1} corresponding to the key intermediate COOH* increased with the accumulation of CO_3^{2-} at 1515 cm^{-1},[48,49] while no observable signals can be detected in the dark, indicating the process of photocatalytic CO_2 reduction. More critically, the characteristic peak of CO* at 2073 cm^{-1} can be clearly

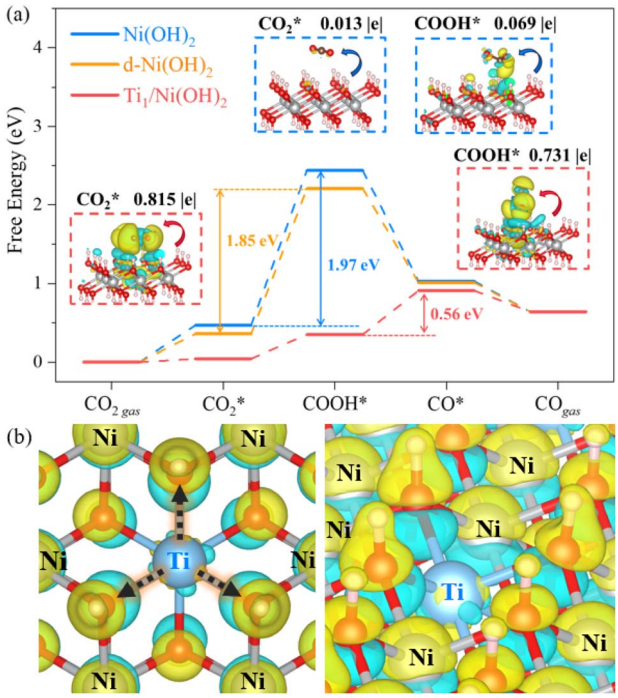

Fig. 4 (a) Energy profiles of CO_2-to-CO conversion on $Ni(OH)_2$, d-$Ni(OH)_2$ and $Ti_1/Ni(OH)_2$. Insets show the electron density difference for $*CO_2$ and *COOH adsorption on $Ni(OH)_2$ (blue frame) and $Ti_1/Ni(OH)_2$ (red frame). Yellow and cyan represent electron accumulation and loss, respectively. (b) Top view and side view for the electron density difference of $Ti_1/Ni(OH)_2$.

identified,[50] demonstrating the altered RDS and the efficient formation of CO.

Furthermore, we confirmed that the intensified interaction between $Ti_1/Ni(OH)_2$ and intermediates results from the substantial charge transfers from the catalyst to the adsorbate (0.815|*e*| for CO_2^* and 0.731|*e*| for COOH*), which were significantly larger than those observed in $Ni(OH)_2$ (0.013|*e*| for CO_2^* and 0.069|*e*| for COOH*, insets of Fig. 4a). According to the electron density difference, the introduction of single Ti sites led to electron donation to the adjacent –OH groups (Fig. 4b and S27†), thus increasing their electron density and resulting in amplified charge transfer from the –OH group to the adsorbates. Overall, the introduction of single Ti sites in $Ti_1/Ni(OH)_2$ effectively regulates the electronic structure and enhances intermediate adsorption on catalysts, thereby decreasing ΔG of the RDS and eventually leading to boosted performance in photocatalytic CO_2 reduction.

Conclusions

In conclusion, through defect engineering, a Ti SAC was successfully constructed on a metal hydroxide support for the first time. By transplanting the TiO_6 octahedron unit from anatase TiO_2, the obtained $Ti_1/Ni(OH)_2$ exhibited significantly enhanced photocatalytic CO_2 reduction activity by more than 30 times compared to pristine $Ni(OH)_2$. According to the mechanistic study, the promoted photocatalytic performance can be attributed to the enhanced affinity to key intermediates and modified electronic structures brought by isolated Ti sites. This work has broadened the scope of single-atom catalysts in early transition metals and provided a useful strategy in photocatalyst design and modification with enhanced performance for CO_2 reduction.

Data availability

The data that support the findings of this study are included in the paper and the ESI.†

Author contributions

Q. X. designed the research. N.-Y. H. performed syntheses and measurements. N.-Y. H., D. C. and Y.-T. Z. performed basic characterization. B. S. performed XAS analysis. W. W. performed EPR measurements. B. L. and L. L. conducted DFT calculations. D. W. and M. G. performed HAADF-STEM measurement. N.-Y. H., B. L., L. L. and Q. X. wrote the manuscript.

Conflicts of interest

There are no conflicts to declare.

Acknowledgements

This work was supported by the National Key Research and Development Project (2023YFA1506601), Guangdong Grants (2021ZT09C064), Shenzhen Key Laboratory of Micro/Nano-Porous Functional Materials (SKLPM) (ZDSYS21210709112802010) and Training Program of the Major Research Plan of the National Natural Science Foundation of China (92270103). The authors acknowledge the assistance of the Pico Center at the Southern University of Science and Technology Core Research Facilities. The theoretical calculations were supported by Center for Computational Science and Engineering at Southern University of Science and Technology. The *in situ* FTIR measurements were supported by Prof. Pei-Qin Liao and Hui-Ying Chen at Sun Yat-sen University.

Notes and references

1 D. I. Armstrong McKay, A. Staal, J. F. Abrams, R. Winkelmann, B. Sakschewski, S. Loriani, I. Fetzer, S. E. Cornell, J. Rockström and T. M. Lenton, *Science*, 2022, **377**, eabn7950.
2 L. Al-Ghussain, *Environ. Prog. Sustain.*, 2019, **38**, 13–21.
3 D.-D. Zhou, X.-W. Zhang, Z.-W. Mo, Y.-Z. Xu, X.-Y. Tian, Y. Li, X.-M. Chen and J.-P. Zhang, *EnergyChem*, 2019, **1**, 100016.
4 C. Zhou, J. Chen, J. Zhao, Y. Meng, Z. Li, X. Meng and J. Wang, *Renewables*, 2024, **2**, 89–110.
5 N.-Y. Huang, Z.-Y. Chen, F.-L. Hu, C.-Y. Shang, W. Wang, J.-R. Huang, C. Zhou, L. Li and Q. Xu, *Nano Res.*, 2023, **16**, 7756–7760.

6 N.-Y. Huang, Y.-T. Zheng, D. Chen, Z.-Y. Chen, C.-Z. Huang and Q. Xu, *Chem. Soc. Rev.*, 2023, **52**, 7949–8004.
7 K. Sun, Y. Qian and H.-L. Jiang, *Angew. Chem., Int. Ed.*, 2023, **62**, e202217565.
8 Y. Wang, E. Chen and J. Tang, *ACS Catal.*, 2022, **12**, 7300–7316.
9 X. Jiao, K. Zheng, L. Liang, X. Li, Y. Sun and Y. Xie, *Chem. Soc. Rev.*, 2020, **49**, 6592–6604.
10 J. Di, G. Hao, G. Liu, J. Zhou, W. Jiang and Z. Liu, *Coord. Chem. Rev.*, 2023, **482**, 215057.
11 Y.-H. Luo, L.-Z. Dong, J. Liu, S.-L. Li and Y.-Q. Lan, *Coord. Chem. Rev.*, 2019, **390**, 86–126.
12 D. Feng, X. Li, Y. Liu, X. Chen and S. Li, *Renewables*, 2023, **1**, 485–513.
13 H. Rao, L. C. Schmidt, J. Bonin and M. Robert, *Nature*, 2017, **548**, 74.
14 Z. Guo, G. Chen, C. Cometto, B. Ma, H. Zhao, T. Groizard, L. Chen, H. Fan, W.-L. Man, S.-M. Yiu, K.-C. Lau, T.-C. Lau and M. Robert, *Nat. Catal.*, 2019, **2**, 801–808.
15 N.-Y. Huang, B. Li, D. Wu, Z.-Y. Chen, B. Shao, D. Chen, Y.-T. Zheng, W. Wang, C. Yang, M. Gu, L. Li and Q. Xu, *Angew. Chem., Int. Ed.*, 2024, **63**, e202319177.
16 S. Dai, T. Kajiwara, M. Ikeda, I. Romero-Muñiz, G. Patriarche, A. E. Platero-Prats, A. Vimont, M. Daturi, A. Tissot, Q. Xu and C. Serre, *Angew. Chem., Int. Ed.*, 2022, **61**, e202211848.
17 P. M. Stanley, V. Ramm, R. A. Fischer and J. Warnan, *Nat. Syn.*, 2024, **3**, 307–318.
18 X. Li, J. Yu, M. Jaroniec and X. Chen, *Chem. Rev.*, 2019, **119**, 3962–4179.
19 Y. Zhang, H. Liu, F. Gao, X. Tan, Y. Cai, B. Hu, Q. Huang, M. Fang and X. Wang, *EnergyChem*, 2022, **4**, 100078.
20 N.-Y. Huang, H. He, S. Liu, H.-L. Zhu, Y.-J. Li, J. Xu, J.-R. Huang, X. Wang, P.-Q. Liao and X.-M. Chen, *J. Am. Chem. Soc.*, 2021, **143**, 17424–17430.
21 L. Wang, W. Chen, D. Zhang, Y. Du, R. Amal, S. Qiao, J. Wu and Z. Yin, *Chem. Soc. Rev.*, 2019, **48**, 5310–5349.
22 C. Gao, J. Low, R. Long, T. Kong, J. Zhu and Y. Xiong, *Chem. Rev.*, 2020, **120**, 12175–12216.
23 P. Liu, Z. Huang, X. Gao, X. Hong, J. Zhu, G. Wang, Y. Wu, J. Zeng and X. Zheng, *Adv. Mater.*, 2022, **34**, 2200057.
24 J.-R. Huang, X.-F. Qiu, Z.-H. Zhao, H.-L. Zhu, Y.-C. Liu, W. Shi, P.-Q. Liao and X.-M. Chen, *Angew. Chem., Int. Ed.*, 2022, **61**, e202210985.
25 H. Ou, S. Ning, P. Zhu, S. Chen, A. Han, Q. Kang, Z. Hu, J. Ye, D. Wang and Y. Li, *Angew. Chem., Int. Ed.*, 2022, **61**, e202206579.
26 H. Shi, Y. Liang, J. Hou, H. Wang, Z. Jia, J. Wu, F. Song, H. Yang and X. Guo, *Angew. Chem., Int. Ed.*, 2024, e202404884.
27 H. Ou, G. Li, W. Ren, B. Pan, G. Luo, Z. Hu, D. Wang and Y. Li, *J. Am. Chem. Soc.*, 2022, **144**, 22075–22082.
28 Y.-S. Wei, M. Zhang, R. Zou and Q. Xu, *Chem. Rev.*, 2020, **120**, 12089–12174.
29 C.-C. Hou, H.-F. Wang, C. Li and Q. Xu, *Energy Environ. Sci.*, 2020, **13**, 1658–1693.
30 Z. Wang, H. Niu, T. Wu, S. Ding, B. Yu Xia and Y. Su, *Renewables*, 2024, **2**, 213–221.
31 X. Jia, Q. Meng, R. Zheng, X. Liu, Y. Zhao, C. Liu, M. Xiao and W. Xing, *Renewables*, 2023, **1**, 694–719.
32 L.-J. Yuan, X.-L. Sui, H. Pan and Z.-B. Wang, *Renewables*, 2023, **1**, 514–540.
33 S. Kaushik, D. Wu, Z. Zhang, X. Xiao, C. Zhen, W. Wang, N.-Y. Huang, M. Gu and Q. Xu, *Adv. Mater.*, 2024, **36**, 2401163.
34 S. K. Kaiser, Z. Chen, D. Faust Akl, S. Mitchell and J. Pérez-Ramírez, *Chem. Rev.*, 2020, **120**, 11703–11809.
35 T. Takata, J. Jiang, Y. Sakata, M. Nakabayashi, N. Shibata, V. Nandal, K. Seki, T. Hisatomi and K. Domen, *Nature*, 2020, **581**, 411–414.
36 J. Schneider, M. Matsuoka, M. Takeuchi, J. Zhang, Y. Horiuchi, M. Anpo and D. W. Bahnemann, *Chem. Rev.*, 2014, **114**, 9919–9986.
37 S. Kreft, D. Wei, H. Junge and M. Beller, *EnergyChem*, 2020, **2**, 100044.
38 Y. Ma, X. Wang, Y. Jia, X. Chen, H. Han and C. Li, *Chem. Rev.*, 2014, **114**, 9987–10043.
39 Y. Wang, H. Liu, Q. Shi, Z. Miao, H. Duan, Y. Wang, H. Rong and J. Zhang, *Angew. Chem., Int. Ed.*, 2024, **63**, e202404911.
40 C. Zhang, S. Liang, W. Liu, F. T. Eickemeyer, X. Cai, K. Zhou, J. Bian, H. Zhu, C. Zhu, N. Wang, Z. Wang, J. Zhang, Y. Wang, J. Hu, H. Ma, C. Xin, S. M. Zakeeruddin, M. Grätzel and Y. Shi, *Nat. Energy*, 2021, **6**, 1154–1163.
41 S. Tang, X. Yin, G. Wang, X. Lu and T. Lu, *Nano Res.*, 2019, **12**, 457–462.
42 A. Pei, G. Li, L. Zhu, Z. Huang, J. Ye, Y.-C. Chang, S. M. Osman, C.-W. Pao, Q. Gao, B. H. Chen and R. Luque, *Adv. Funct. Mater.*, 2022, **32**, 2208587.
43 X. Chen, J. Wan, J. Wang, Q. Zhang, L. Gu, L. Zheng, N. Wang and R. Yu, *Adv. Mater.*, 2021, **33**, 2104764.
44 J. Zhang, X. Wu, W.-C. Cheong, W. Chen, R. Lin, J. Li, L. Zheng, W. Yan, L. Gu, C. Chen, Q. Peng, D. Wang and Y. Li, *Nat. Commun.*, 2018, **9**, 1002.
45 Y.-j. Wu, J. Yang, T.-x. Tu, W.-q. Li, P.-f. Zhang, Y. Zhou, J.-f. Li, J.-t. Li and S.-G. Sun, *Angew. Chem., Int. Ed.*, 2021, **60**, 26829–26836.
46 Z. Chen, L. Liang, H. Yuan, H. Liu, P. Wu, M. Fu, J. Wu, P. Chen, Y. Qiu, D. Ye and L. Chen, *Appl. Catal., B*, 2021, **298**, 120507.
47 M. D'Arienzo, M. V. Dozzi, M. Redaelli, B. D. Credico, F. Morazzoni, R. Scotti and S. Polizzi, *J. Phys. Chem. C*, 2015, **119**, 12385–12393.
48 Y.-N. Gong, J.-H. Mei, W.-J. Shi, J.-W. Liu, D.-C. Zhong and T.-B. Lu, *Angew. Chem., Int. Ed.*, 2024, **63**, e202318735.
49 X. Zu, Y. Zhao, X. Li, R. Chen, W. Shao, L. Li, P. Qiao, W. Yan, Y. Pan, Q. Xu, J. Zhu, Y. Sun and Y. Xie, *Angew. Chem., Int. Ed.*, 2023, **62**, e202215247.
50 H. Huang, J. Zhao, B. Weng, F. Lai, M. Zhang, J. Hofkens, M. B. J. Roeffaers, J. A. Steele and J. Long, *Angew. Chem., Int. Ed.*, 2022, **61**, e202204563.